

REGULAR PAPER

# Propulsion integration study of civil aero-engine nacelles

F. Tejero<sup>1</sup> , D. MacManus<sup>1</sup>, I. Goulos<sup>1</sup> and C. Sheaf<sup>2</sup>

<sup>1</sup>Centre for Propulsion Engineering, School of Aerospace, Transport and Manufacturing, Cranfield University, Bedfordshire, MK43 0AL, United Kingdom and <sup>2</sup>Rolls-Royce PLC., P.O. box 31, Derby, DE24 8BJ, United Kingdom

**Corresponding author:** F. Tejero; Email: [f.tejero@cranfield.ac.uk](mailto:f.tejero@cranfield.ac.uk)

**Received:** 17 October 2022; **Revised:** 13 April 2023; **Accepted:** 18 May 2023

**Keywords:** propulsion; integration; UHBPR; aero-engine; nacelle

## Abstract

It is envisaged that future civil aero-engines will operate with ultra-high bypass ratios to reduce the specific fuel consumption. To achieve the expected benefits from the new engine cycles, these new powerplants may mount compact nacelles. For these new configurations the aerodynamic coupling between the powerplant and the airframe may increase. For this reason, it is required to quantify and further understand the effects of aircraft integration for compact aero-engine nacelles. This study provides an insight of the changes in flow aerodynamics as well as quantification of the most relevant performance metrics of the powerplant, airframe and the combined aircraft system across a range of different installation positions. Relative to a conventional architecture, there is an aerodynamic benefit in net vehicle force of about 1.2% for a compact powerplant when installed in forward positions. This is the same improvement that was identified when the aero-engine nacelles were in isolation. However, for close-coupled installation positions, the aerodynamic benefit in net vehicle force erodes to 0.44% due to the larger effects of aircraft integration on compact nacelles.

## Nomenclature

### Roman symbol

$L$	Length
$M$	Mach number
$r$	radius
$V$	velocity

### Acronyms

$CRM$	Common Research Model
$GPF$	Gross propulsive force
$MFCR$	Mass flow capture ratio
$NPF$	Net propulsive force
$NVF$	Net vehicle force
$UHBPR$	Ultra high bypass ratio

### Greek Symbol

$\eta$	Wing cross-section
$\phi$	Force in drag domain
$\psi$	Nacelle azimuthal angle
$\theta$	Force in thrust domain

**Superscripts and subscripts**

$\infty$	free-stream
<i>hi</i>	highlight
<i>nac</i>	nacelle
<i>post</i>	post-exit
<i>pre</i>	prepre-entry

**1.0 Introduction**

The housing components of an aero-engine are the intake, nacelle and separate jet exhaust [1]. Within the context of ultra-high bypass ratio (UHBPR) aero-engine nacelles, it is envisaged that the bulk parameters of highlight radius, trailing edge radius, nacelle length and maximum radius will be reduced as much as possible [2]. For a viable aerodynamic design, this results in a reduction in wetted area which may be accompanied by a reduction in nacelle drag. The term compact used throughout this work refers to this design philosophy for UHBPR turbofan nacelles. Future civil aero-engines are likely to have larger bypass ratios (BPR) [1] and lower fan pressure ratios (FPR) than current architectures. This trend is to improve the propulsive efficiency [3] and reduce the engine specific fuel consumption. It is anticipated that future turbofans will have BPR between 14 and 21 [4]. This will result in larger fan diameters and a concomitant increment in nacelle size, overall weight and aerodynamic interactions between the airframe and the aero-engine [5]. Therefore, there is a requirement to design compact turbofan architectures that will not counterbalance the benefits obtained from the new engine cycles [4]. Due to the large fan diameters of future civil aero-engines, these new podded underwing configurations are expected to be installed in close-coupled positions [1]. This is to fulfill the mechanical design constraints of the engine-airframe integration, which include pylon structural considerations, wing flutter and ground clearance requirements [4].

Previous research have investigated the challenges of propulsion integration for ultra-high bypass ratio turbofans [4, 6–10]. Dagget [4] studied the effect of varying the BPR from 11.5 to 21.5 on the specific fuel consumption. It was concluded that an engine with moderate BPR = 14.5 achieved the lowest specific fuel consumption and operating cost when installation effects were taken into account. Wiart et al. [6] evaluated the effects of installation position in a UHBPR aero-engine nacelle with a benign normalised nacelle length ( $L_{nac}$ ) to highlight radius ( $r_{hi}$ ) of  $L_{nac}/r_{hi} = 4.0$ . Different axial and vertical positions were considered for a transonic flight Mach number of  $M = 0.82$ . Relative to the most forward installation position with the largest vertical offset, the closest installation position to the wing resulted in a penalty of 2.5% on the overall aircraft drag. The investigation only evaluated forward installation positions in which the trailing edge of the nacelle top aero-line was located upstream of the wing leading edge. Similarly, Sibilli et al. [7] investigated the influence of engine installation position on mission fuel burn. The study was based on a simplified nacelle design and only changes on the horizontal positioning were considered. The most forward position resulted in a mission fuel burn reduction of 3.7% with respect to the reference installation position. Silva et al. [9] compared the aerodynamic performance between over-the-wing and under-the-wing mounted nacelle configurations. It was found that for the same aircraft lift coefficient, the over-the-wing case required a larger angle-of-attack than the under-the-wing arrangement. For the trimmed condition, the installation drag of the over-the-wing architecture was 19.7 drag counts higher than the podded under-wing one. Other studies have considered the nacelle design process by taking into account aircraft integration aspects [11, 12] For example, Li et al. [11] carried out the aerodynamic design optimisation of the nacelle and pylon position on the DLR-F6 aircraft. The study was based on a nacelle throughflow configuration. Relative to a baseline position, it was concluded that the overall aircraft drag could be ‘reduced by 1.1% when the nacelle was installed in a more forward position. Tejero et al. [12] optimised a powered aero-engine nacelle in which the effects of installation were considered during the design process. This was enabled by the combination of data-driven methods that included dimensionality reduction and multi-fidelity techniques. Relative to a baseline configuration, the process yielded a new nacelle with an increment in the normalised net

vehicle force of 0.65%. This approximately equates to an equivalent reduction in cruise fuel burn. To minimise the overall nacelle drag contribution to the aircraft, recent works have also focused in designing natural laminar nacelles [13, 14]. For instance, Zhang et al. [13] carried out aerodynamic comparisons between isolated and installed configurations to derive design guidelines for transonic natural laminar flow nacelles. The study only considered a forward installation position.

There is a clear need to design compact aero-engine nacelles that will not erode the benefits obtained from the new engine cycles. In this respect, it is required to understand the changes in the transonic flow aerodynamics associated to compact aero-engine nacelles and their propulsion integration challenges. Whilst previous studies in the open literature have considered the effects of aircraft integration for ultra-high bypass ratio turbofans, the analysis was mainly based on benign installation positions. As such, there is a clear need to extend the aerodynamic analysis to a wider range of positions for this new design challenge. The novelty of this work lies in the assessment and quantification of the aerodynamic feasibility of compact UHBPR aero-engines when the effects of aircraft integration are considered. This study provides for the first time guidelines of potential aerodynamic penalties that may arise due to the expected requirements for close-coupled installation positions. The aerodynamic performance metrics are summarised for the integrated airframe-engine system as well as its constituent components to identify the dominant metrics as a function of installation position. This work also presents the changes in the flow characteristics along the powerplant and airframe, which enables the better understanding of the challenges for propulsion integration of future UHBPR aero-engines. The results are compared with the aerodynamic performance of a conventional turbofan and the aerodynamic feasibility of installed compact UHBPR architectures is assessed.

## 2.0 Methodology

The aero-engine nacelles used in this research have been designed with a well-established multi-point, multi-objective optimisation method. The approach has been successfully used in the past to identify the limits of the feasible design space of compact nacelles [2], quantify the isolated aerodynamic benefits of compact nacelles with respect to conventional configurations [15] and assess the nacelle drag trade-off between intake compactness and nacelle length [16]. A thorough description of the method and computational approach has been provided in the past [2, 15, 16] and, as such, it is not presented here. Once the isolated powerplants were designed and optimised, they were installed into an airframe for the analysis of the integrated propulsion system.

The aerodynamic analysis of the installed aero-engine is performed with the NASA Common Research Model (CRM) [17]. This airframe is representative of a conventional commercial transport aircraft with a cruise flight Mach number of 0.85 at  $C_L = 0.5$ . The full configuration comprises the CRM airframe [17, 18], nacelle [2], intake [19], exhaust [20] and pylon [21] (Fig. 1). The exhaust after-body is designed to be conical. The after-body length and half-cone angles are selected on the basis of minimising over-acceleration of the bypass exhaust flow on the core after-body [21]. This reduces the shock strength within the exhaust flow downstream of the bypass nozzle exit. The design of the core nozzle and plug is carried out on the basis of alleviating any flow separation on the pylon heat-shield downstream of the core nozzle exit. To establish the flow-capacities for sizing the bypass and core exhaust nozzles, the engine cycle was designed with a zero-dimensional cycle modelling tool [22] to provide representative conditions for an UHBPR engine [20]. The pylon is constructed as a series of aerofoil sections that are mounted on the vertical direction and designed to avoid adverse flow features [21]. The aero-engine is integrated in the same spanwise podded under-wing installation position as the throughflow nacelle of the CRM benchmark test case [23] and with the same values of pitch and toe angles.

A hybrid meshing approach is used with structured prism layers near the viscous walls and tetrahedral elements for the remainder of the domain. The grid generation follows the guidelines from the 4<sup>th</sup> AIAA Drag Prediction Workshop (DPW) [24]. The first layer height is adjusted to satisfy a  $y^+$  of approximately 1 on the non-slip walls, i.e. CRM fuselage, wing, tail-plane and powerplant. A grid independence

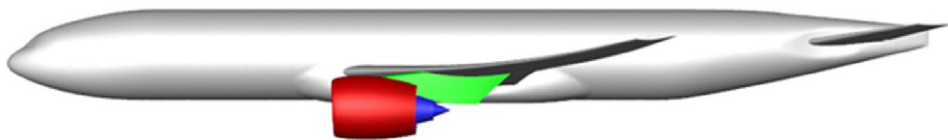


**Figure 1.** NASA Common Research Model with optimised drooped and scarfed non-axisymmetric nacelle (red), separate jet exhaust system (blue) and pylon (green).

analysis was carried out for mid-cruise conditions ( $M = 0.85$  at  $C_L = 0.5$ ) in which three meshes were considered with approximately  $60 \times 10^6$ ,  $120 \times 10^6$  and  $240 \times 10^6$  elements. For the medium mesh, the grid convergence index of the powerplant's net propulsive force, and the airframe drag was approximately 0.5% and 0.1%, respectively. As such, the grid with  $120 \times 10^6$  elements was selected for this investigation. The numerical approach has been validated with the experimental data from the NASA Common Research Model (CRM) [23]. The assessment of the computational method was based on the wind tunnel conditions of a wing chord  $Re = 5 \times 10^6$ , flight Mach number  $M = 0.85$  and  $C_L = 0.5$ . The computational method overpredicts by 14 and 16 drag counts the airframe drag on the clean wing CRM and the throughflow nacelle CRM configurations, respectively. Similar overpredictions have been reported in other studies [25]. A detailed description of the method's validation has been provided by Goulos et al. [26].

The compressible steady-state flow-field is computed with a double-precision density-based Favre-Averaged Navier-Stokes solver. The  $k-\omega$  Shear-Stress Transport (SST) two-equation turbulence model [27] is used. The flow-field gradients are calculated with a Green-Gauss node-based method, and a second-order upwind scheme for the spatial discretisation of the variables is employed. The dynamic viscosity is calculated with Sutherland's law. The converge criteria is based on a reduction of at least four orders of magnitude of the continuity, velocity, energy, turbulent kinetic energy and specific turbulent dissipation rate. The aircraft drag and lift, massflow through the engine and forces on the engine-walls were monitored and their variation was lower than 0.01% for the last 100 iterations.

Regarding the boundary conditions, the farfield is modelled with a pressure-farfield condition in which the Mach number, the static pressure and the static temperature are specified. The fan-face is defined with a target massflow pressure-outlet condition that is calculated from the specified massflow capture ratio [2]. The exhaust inlets are set with pressure inlets by specifying the total pressure and temperature. A non-slip adiabatic condition is imposed for the fuselage, wing, tail-plane and powerplant walls.

### 2.1 Thrust-drag bookkeeping

The thrust-drag bookkeeping accounting used in this investigation is based on the method developed by Goulos et al. [26] for combined airframe and powerplant systems (Fig. 2). It considers that the forces are positive in downstream direction and the gauge forces are positive upstream of the control volume boundaries. The streamtube-external force, i.e. drag domain, is represented by  $\phi$ , the streamtube-internal force, i.e. thrust domain, is represented by  $\theta$ . The gauge stream forces across the boundaries ( $F_G$ ) are calculated by integrating the pressure and momentum terms over the area of interest and the forces exerted on the engine walls are computed by integrating the pressure and viscous terms [28]. Within this study, the forces are solved in the aerodynamic drag axes (Fig. 2).

The modified gross propulsive force ( $GPF^*$ ) accounts for the aerodynamic thrust force generated on the nozzle afterbodies (Equation (1)). The modified velocity coefficient ( $C_v$ ) is defined as the ratio of the modified gross propulsive force and the ideal thrust from an isentropic fully expanded exhaust momentum flux [26] (Equation (2)). The cycle modified gross propulsive force ( $(GPF^*)_{ins-cycle}$ ) is calculated by scaling the ideal exhaust moment efflux, which is based on the associated engine cycle obtained from a thermodynamic model [22], with the modified velocity coefficient (Equation (3)).

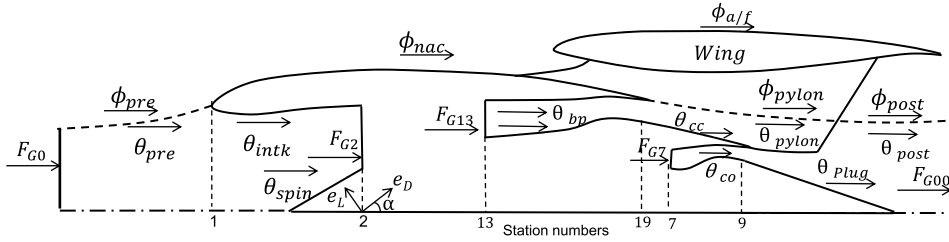


Figure 2. Thrust and drag bookkeeping for combined airframe-engine systems.

$$GPF^*_{ins} = F_{G13} + F_{G7} - (\theta_{bp} + \theta_{cc} + \theta_{co} + \theta_{plug} + \theta_{pylon}), \tag{1}$$

$$C^*_v = \frac{GPF^*_{ins}}{\dot{m}_{13} V_{13}^{ideal} + \dot{m}_7 V_7^{ideal}}, \tag{2}$$

$$GPF^*_{ins-cycle} = C^*_v (\dot{m}_{13}^{cycle} V_{13}^{ideal} + \dot{m}_7^{cycle} V_7^{ideal}). \tag{3}$$

The modified near-field method [2] is used to extract the modified nacelle drag ( $D^*_{nac}$ ). This term is the sum of forces on the pre-entry streamtube ( $\phi_{pre}$ ), fangcowl aerodynamic force ( $\phi_{pre}$ ) and the aerodynamic force exerted on the part of the pylon surface that is not wetted by the exhaust jet ( $\phi_{pylon}$ ) (Equation (4)). The pylon surface is divided by the the streamline of total temperature ( $T_0$ ) to distinguish between the thrust ( $\phi_{pylon}$ ) and drag ( $\phi_{pylon}$ ) domain of the pylon [26].

$$D^*_{nac} = \phi_{pre} + \phi_{nac} + \phi_{pylon}. \tag{4}$$

Subsequently, the corrected installed net propulsive force ( $NPF_{ins-cycle}$ ) is derived (Equation (5)):

$$NPF_{ins-cycle} = GPF^*_{ins-cycle} - F_{G,0} - D^*_{nac}. \tag{5}$$

The overall aerodynamic performance of the combined airframe and powerplant system is reported in this study in terms of net vehicle force (NVF), Equation (6), where the airframe drag ( $D_{A/F}$ ) contains the drag terms of the fuselage, wing and tailplane.

$$NVF = NPF_{ins-cycle} - D_{A/F}. \tag{6}$$

### 3.0 Results and discussions

This work considers two powerplant configurations: a compact architecture that is representative of a future civil aero-engine with  $L_{nac}/r_{hi} = 3.1$  and a conventional turbofan with  $L_{nac}/r_{hi} = 3.8$ . The configurations are derived for long-range applications with a mid-cruise flight Mach number of 0.85. The aero-engine nacelles were designed through a multi-point, multi-objective optimisation routine (Section 3.1) and subsequently installed into the airframe to assess the impact of engine installation position for 10 podded under-wing positions (Section 3.2).

#### 3.1 Multi-point, multi-objective aerodynamic nacelle optimisation

For the two powerplants of interest, i.e.  $L_{nac}/r_{hi} = 3.1$  and  $L_{nac}/r_{hi} = 3.8$ , the aerodynamic multi-point, multi-objective optimisation was carried out with the method developed by Tejero et al. [16, 29]. The design process considered different conditions within the cruise segment. In this respect, the sensitivity to changes in flight Mach number and massflow capture ratio were evaluated during the optimisation routine. The process resulted in two independent Pareto optimal set of aero-engine nacelles. A thorough description of the outcomes of both multi-point, multi-objective has been previously provided [30] and, as such, it is omitted in this work. From the Pareto fronts, a compact ( $L_{nac}/r_{hi} = 3.1$ ) and conventional aero-engine ( $L_{nac}/r_{hi} = 3.8$ ) were downselected. To characterise the aerodynamic behaviour of

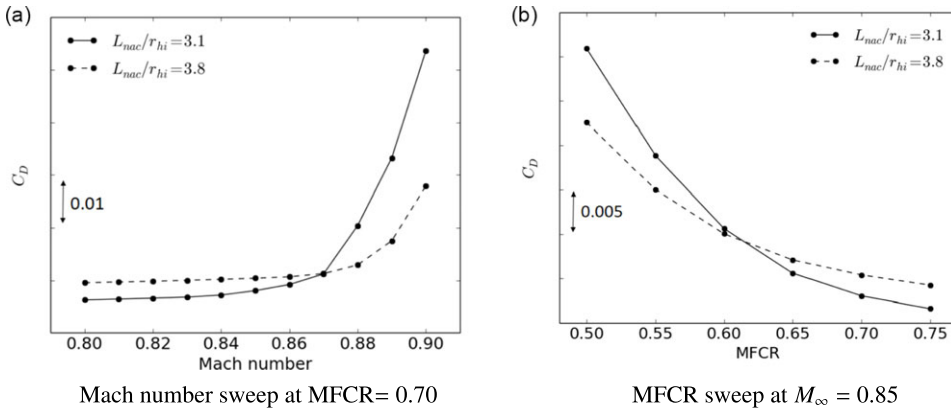


**Figure 3.** Nacelle drag comparison between both aero-engines.

the selected designs, both were evaluated at different aerodynamic operating conditions of Mach number and MFCR. Figure 3(a) presents the drag-rise curve at constant mid-cruise MFCR = 0.70, which highlights how sharp the increase of nacelle drag coefficient (Equation (7)) can be for a compact configuration. Whilst there is a nacelle drag benefit of 7.4% at design point ( $M_\infty = 0.85$ ) and the nacelle drag is slightly reduced at  $M_\infty = 0.87$ , a further increment in flight Mach number to  $M_\infty = 0.88$  reveals the sensitivity of this design with a penalty in nacelle drag of about 23%. Similarly, the configuration with  $L_{nac}/r_{hi} = 3.1$  has larger nacelle drag penalties than the  $L_{nac}/r_{hi} = 3.8$  design as the massflow capture ratio decreases (Fig. 3(b)).

$$C_D = \frac{D_{nac}}{\frac{1}{2}\rho_\infty V_\infty^2 A_{hi}} = \frac{\phi_{pre} + \phi_{nac} + \phi_{post}}{\frac{1}{2}\rho_\infty V_\infty^2 A_{hi}} \quad (7)$$

### 3.2 Installation effects on compact UHBPR aero-engine nacelles

The aerodynamic design and analysis of installed aero-engines has been carried out to quantify the effects of aircraft integration on both optimised aero-engines. This is performed at mid-cruise conditions with a flight Mach number  $M_\infty = 0.85$ , MFCR = 0.70. The aero-engine has a BPR above 15 and an engine cycle to maximise the specific thrust with fan and core nozzle pressure ratios of approximately 2.2 and 1.5, respectively [26]. All the aerodynamic metrics presented in this investigation are reported for a constant  $C_L = 0.5$  [24]. This is achieved by running a localised aircraft incidence sweep and applying a linear interpolation to match the desired lift coefficient.

#### 3.2.1 Effect of installation position on compact aero-engine nacelles

The installation position for a given powerplant shape is a degree of freedom that has a large impact on the overall aircraft performance [6]. Depending on the location of the engine under the wing, the strength of the aerodynamic coupling between the nacelle and the wing will change. Hence, it is important to understand the main flow physics that govern the nacelle aerodynamics for a wide range of positions. In addition, the aerodynamic analysis has to be carried out with a global metric that accounts for the changes on the powerplant and airframe. For this purpose, this study uses the net vehicle force (NVF) as defined in Equation (6). Its constituent metrics are also analysed, i.e.  $NPF_{ins-cycle}$ ,  $D_{a/f}$  and  $D_{nac}^*$ , to provide a better insight of the changes as a function of the installation position of the powerplant. The numerical assessment of installation effects is carried for a total of 10 different installation positions that include forward as well as overlapped locations (Fig. 4). The installation position is defined with

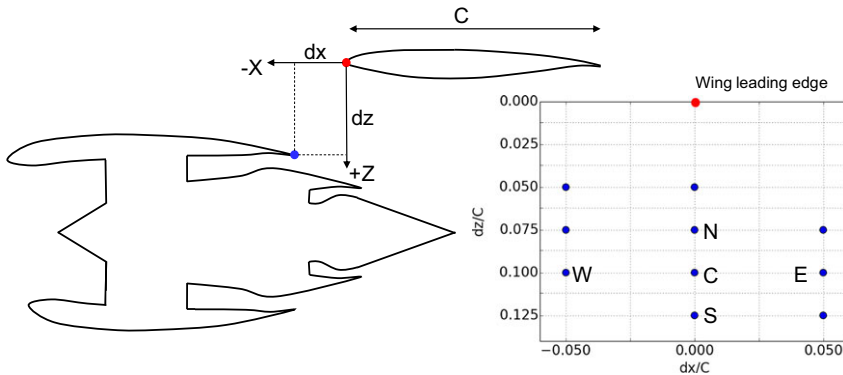
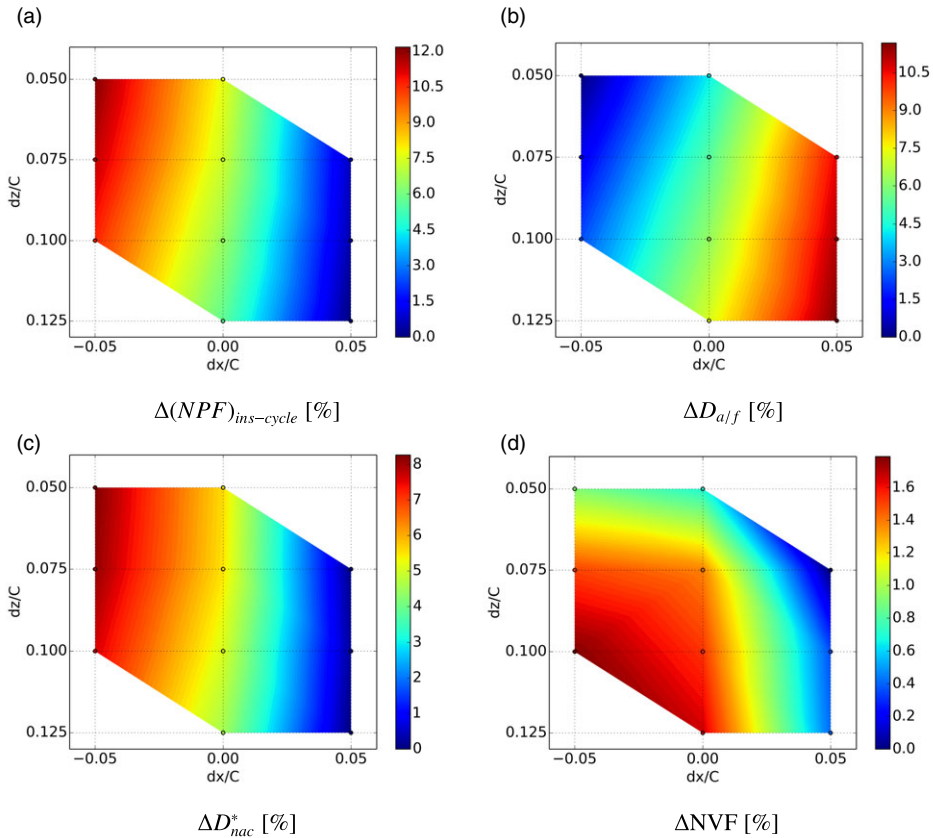


Figure 4. Design space exploration for nacelle installation positions.

the axial and vertical offset from the nacelle top-line trailing edge and the wing leading edge. The distance is normalised with the wing cord ( $c$ ). Three different axial positions are considered with values of  $dx/c = -0.05, 0.0, +0.05$ , which refers to forward, coincident and overlapped locations, respectively. A total of four vertical locations within the range of  $dz/c$  between 0.05 and 0.125 were investigated. Whilst the aerodynamic analysis is carried out for the range of positions showed in Fig. 4, a more detailed aerodynamic analysis is performed for the positions C, N, S, W and E (Fig. 4). This comparison enables the understanding of the two key installation variables of  $dx/c$  and  $dz/c$  on the overall aircraft performance. The installed analysis is initially carried out for the compact aero-engine nacelle with  $L_{nac}/r_{hi} = 3.1$  that was downselected from the isolated multi-point, multi-objective optimisation (Section 3.1).

The different integral values for the thrust and drag contribution on the overall aircraft performance are presented in Fig. 5. The net vehicle force changes across the design space are shown (Fig. 5(d)), as well as its constituent metrics of  $NPF_{ins-cycle}$  (Fig. 5(a)),  $D_{ajf}$  (Fig. 5(b)) and  $D_{nac}^*$  (Fig. 5(c)). All the installation maps are relative to the worst installation position of each metric, and are normalised by the cruise standard net thrust ( $F_N$ ). The net vehicle forces varies by 1.7% (Fig. 5(d)). The best installation position is the most forward with the largest vertical offset relative to the wing ( $dx/c = -0.05$  and  $dz/c = +0.1$ ) and the lowest value of NVF appears at the most close-coupled installation position ( $dx/c = +0.05$  and  $dz/c = +0.075$ ). This is caused by the increment in the interference effects as the powerplant is moved closer to the wing. As the powerplant is overlapped with the wing, its axial location ( $dx/c$ ) has a larger influence on NVF than the vertical offset ( $dz/c$ ). To identify the reasons for the changes on NVF, the metrics of  $NPF_{ins-cycle}$  and  $D_{ajf}$  were also analysed. The installed net propulsive force ( $NPF_{ins-cycle}$ ), which quantifies the overall aerodynamic performance of the aero-engine, varies by 12.0% across the design space (Fig. 5(a)). This is an increment of approximately a factor of 7 with respect to NVF. The lowest values appear for close-coupled installation positions where larger interactions effects between the engine and wing are present. For the range of locations considered, the axial installation position has a first order impact. This performance metric can be subsequently decomposed into the modified gross propulsive force, the inlet momentum and the modified drag (Equation (5)). As there is no variation of the inlet momentum term ( $F_{G,0}$ ), the changes on  $NPF_{ins-cycle}$  are accounted by the balance between the engine's thrust ( $GPF_{ins-cycle}^*$ ) and drag ( $D_{nac}^*$ ). Across the different installation positions, the modified nacelle drag varies by 8% (Fig. 9). The larger penalties are obtained for overlapped positions due to the expected adverse flow features caused by the coupling nacelle/airframe. As for the installed net propulsive force ( $NPF_{ins-cycle}$ ), the axial location ( $dx/c$ ) dominates the changes on modified nacelle drag. Lastly, the airframe drag ( $D_{ajf}$ ) varies by approximately 11.0% across the design space (Fig. 8). As such, the relative changes across the installation positions between the metrics  $NPF_{ins-cycle}$  and  $D_{ajf}$  are similar (Fig 5(a) and (b)). However, their trends are different and there is a benefit on  $D_{ajf}$  as the engine is close-coupled. It is important to note that the angle-of-attack to trim the NASA CRM to the nominal condition of  $C_L = 0.5$  was very similar for the different engine locations. As such, the variability of



**Figure 5.** Variation of airframe-engine aerodynamic performance metrics across the design space for the compact aero-engine nacelle ( $L_{nac}/r_{hi} = 3.1$ ). Results are normalised with the engine net thrust ( $F_N$ ) and are relative to the worst position. Positive values refer to an aerodynamic benefit in the metric.

11.0% is caused by effects of powerplant integration. The airframe drag and net propulsive force have large absolute values but opposite polarity, which results in the relative small variation of NVF across the design space (Fig. 5(d)) due to the both conflicting metrics.

A more detailed analysis of the different aerodynamic performance metrics was carried out to quantify the effect of axial ( $dx/c$ ) and vertical ( $dz/c$ ) installation position (Fig. 5d). Relative to the position C (Fig. 4), the impact of changes on  $dx/c$  are investigated with the positions W and E, and the influence of  $dz/c$  is analysed with the positions N and S (Fig. 6). For example, for the position N there is an increment in net propulsive force of 0.75% and there is a penalty in airframe drag of approximately  $-0.90\%$ . Conversely, the polarity changes for the position S with a penalty in  $NPF_{ins-cycle}$  of about  $-0.81\%$  and an airframe drag benefit of 0.94%. These result in modest variations at an overall aircraft level with changes in NVF of  $-0.15\%$  and  $0.13\%$  for position N and S, respectively. Conversely, an axial movement ( $dx/c$ ) of the powerplant to the positions W and E results in larger aerodynamic changes. For example, the  $NPF_{ins-cycle}$  varies by 4.1% and  $-6.0\%$  for the positions W and E, respectively. For these positions, the airframe drag  $D_{alf}$  presents a penalty of  $-3.9\%$  and a benefit of 4.9%. These conflicting metrics results in a NVF change of  $+0.24\%$  and  $-1.1\%$  for the position W and E, respectively. For the position E, the aerodynamic penalty of the combined airframe/engine system is caused by the large nacelle drag due to the effects of integration for close-coupled positions, Relative to the reference position C, there is a nacelle drag penalty of 4.88% (Fig. 6).

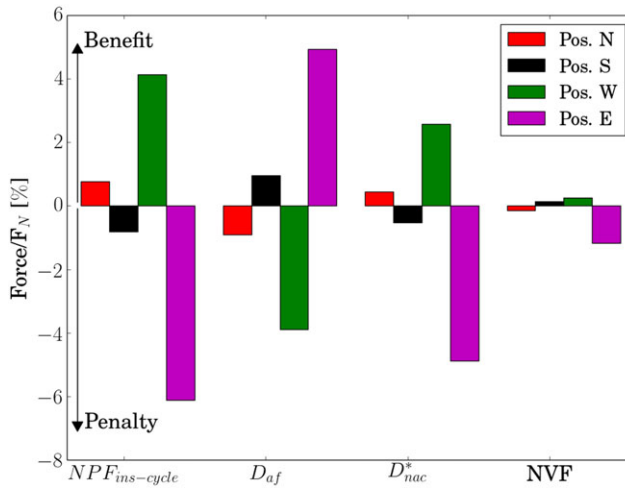


**Figure 6.** Effect of moving the installation position for the compact aero-engine nacelle ( $L_{nac}/r_{hi} = 3.1$ ). Results are relative to position C.

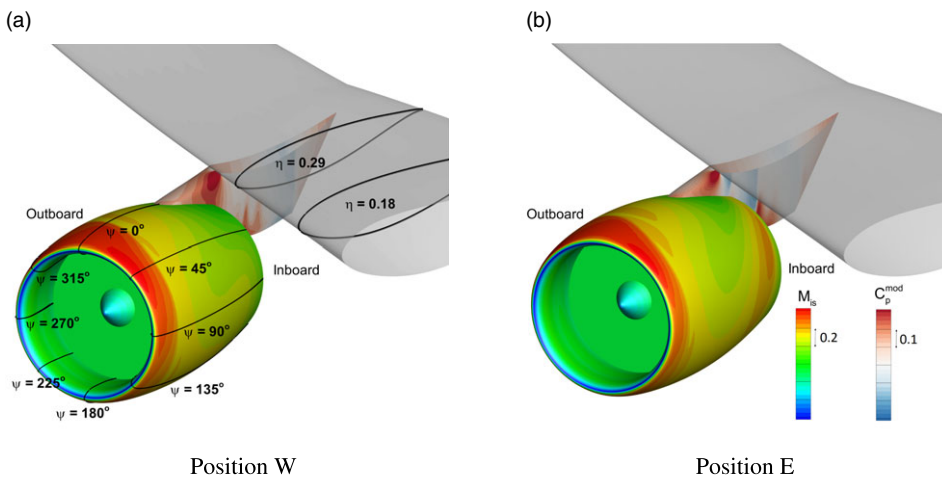


**Figure 7.** Isentropic Mach number distribution on the compact aero-engine nacelle ( $L_{nac}/r_{hi} = 3.1$ ) for the (a) forward and (b) close-coupled installation positions.

To provide an initial insight of the changes on the nacelle aerodynamics as a function of installation position, Fig. 7 shows the contour of isentropic Mach number on the nacelle inboard side for position W and E. It clearly highlights the adverse flow features that can form on the nacelle as the powerplant is close-coupled with the wing. Whilst the nacelle forebody is very similar in both locations (W and E), there is a large acceleration on the nacelle aft-end when it is installed in the position E. This effect is primarily caused by the gully flow between the nacelle and the pressure side of the wing. These flow characteristics results in a penalty of 7.5% on modified nacelle drag when the aero-engine nacelle is installed in the position E with respect to W (Fig. 5(c)).

The nacelle aerodynamics change across the design space of considered installation positions (Fig. 8). For a fixed  $d/z = 0.1$ , there are significant variations on the nacelle flow characteristics by moving the nacelle installation position from  $dx/c = -0.05$  to  $+0.05$ , i.e. from position W to E (Fig. 4). For example, for the inboard top-control aero-line ( $\psi = 45^\circ$ ) the peak and pre-shock Mach number reduce as the

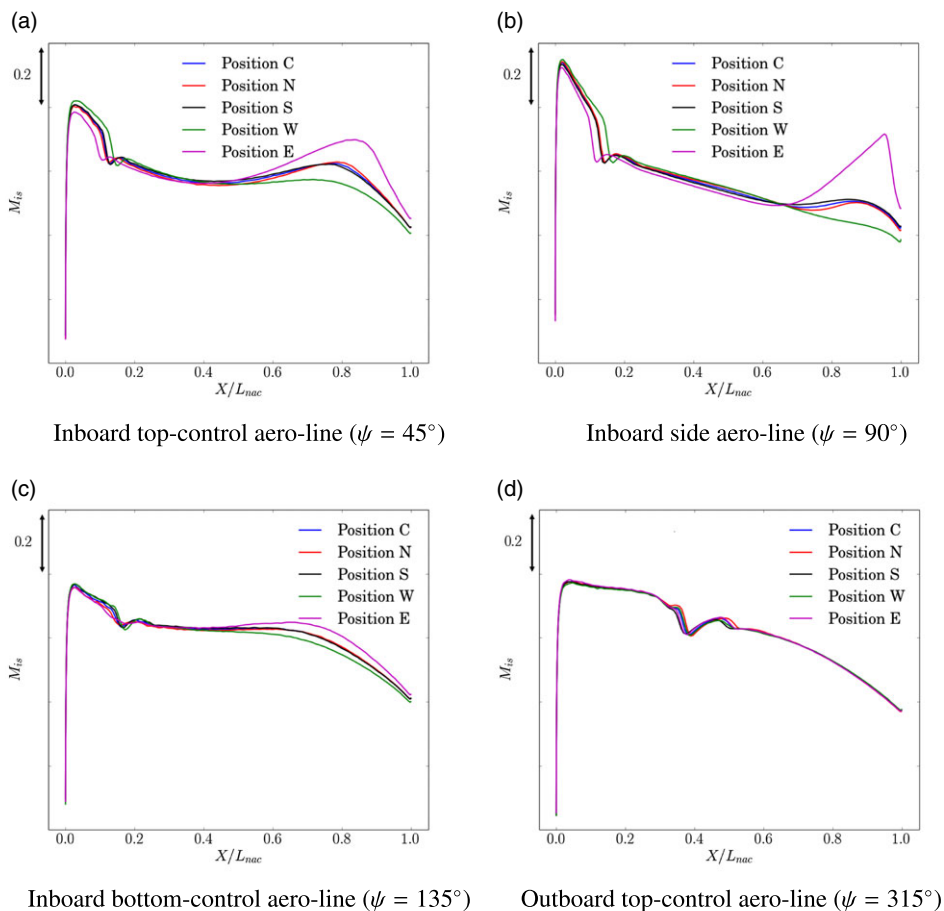


**Figure 8.** Comparison of isentropic Mach number distribution along the aero-engine nacelle for different installation positions.

engine is close-coupled (Fig. 8(a)). In addition, the peak  $M_{is}$  varies by approximately 0.04 and the pre-shock  $M_{is}$  changes by 0.02. More exacerbated changes are found at the nacelle aft-end, where there is a large acceleration with an increment on  $M_{is}$  of 0.14 for the location E with respect W. The locations N, C and S, which assess the effect of vertical offset ( $dz/c$ ), show negligible effects on the nacelle aerodynamics. It highlights the first order impact of the axial installation position ( $dx/c$ ) on the nacelle flow characteristics. Similar findings were identified for the inboard side aero-line ( $\psi = 90^\circ$ ) (Fig. 8(b)), in which a strong shock-wave is formed when the engine is close-coupled in location E. It confirms the expected adverse flow features highlighted above (Fig. 7(b)). Conversely, the isentropic Mach number distribution for the bottom-control aero-line ( $\psi = 135^\circ$ ) are very similar due to the low interaction of this aero-line with the airframe (Fig. 8(c)). Regarding the nacelle outboard side, the aerodynamics are also similar across the different installation positions. For example, Fig. 8(d) shows the comparison for the 5 investigated installation positions (C, N, E, S, W) in the outboard top-control aero-line ( $\psi = 315^\circ$ ) as defined in Fig. 7(a). It is expected that for the outboard aero-lines, the strongest aerodynamic coupling between nacelle and wing is at  $\psi = 315^\circ$ . However, all five installation positions present similar  $M_{is}$  distributions, which demonstrates that the effects of aircraft integration on the outboard nacelle aerodynamics are negligible.

Variations in the powerplant's installation position also result in changes on the wing aerodynamics. In this respect, two wing cross-sections ( $\eta = 0.18$  and  $0.29$  as defined in Fig. 7(a)) are presented

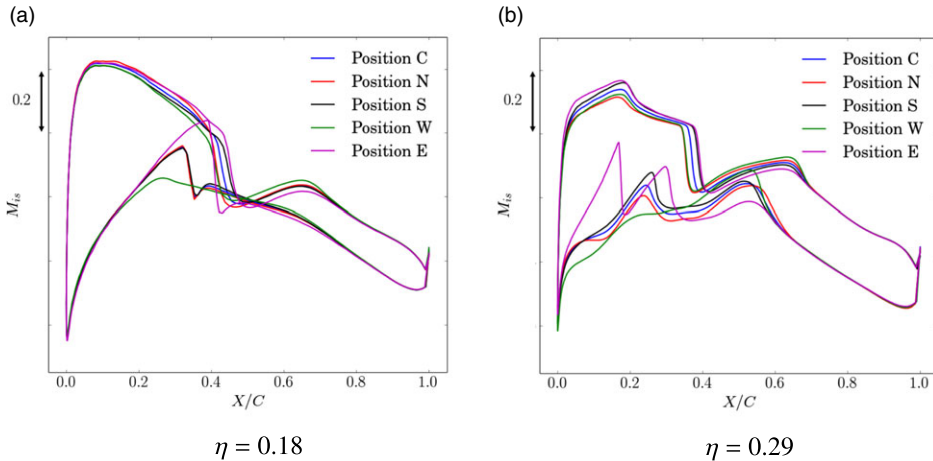


**Figure 9.** Comparison of isentropic Mach number distribution along the CRM wing for different installation positions.

in Fig. 9. For the first one at  $\eta = 0.18$ , the effect of installation position does not have a large impact on the wing’s suction side. For the 5 selected locations the peak and pre-shock  $M_{is}$  are very similar, and the shock location varies within  $x/c = 0.05$ . As it could be expected, more differences arise on the aerodynamics of the wing’s pressure side. Whilst no shock-wave is observed for the most benign installation position of W, the other locations, i.e. C, N, E and S, have a well defined shock. The positions with  $dx/c = 0.0$  (C, N and S) present the same aerodynamics. Relative to these locations the shock strength increases by  $\Delta M_{is} = 0.1$  for the close-coupled position E. For the other wing cross-section with  $\eta = 0.29$ , there are larger aerodynamic differences as a function of the installation position due to the larger effects of powerplant integration (Fig. 9(b)). Position E depicts a change in the shock topology on the pressure side caused by the interactions effects associated to close-coupled installation positions.

### 3.2.2 Impact of aero-engine nacelle architecture

A key aspect of this study is to quantify the expected aerodynamic benefits of installed compact UHBPR aero-engine nacelles with respect to conventional architectures. For this reason, the effects of aircraft integration for the conventional configuration ( $L_{nac}/r_{hi} = 3.8$ ), optimised in Section 3.1, were also evaluated. Although a similar aerodynamic analysis as previously conducted for the compact nacelle could be carried out for the conventional configuration, a more meaningful study is to compare the changes on the aerodynamic performance between the two architectures as a function of installation position. In this respect, Fig. 10 presents the difference on normalised NVF,  $NPF_{ins-cycle}$ ,  $D_{aff}$  and  $D_{nac}^*$  between the compact aero-engine nacelle ( $L_{nac}/r_{hi} = 3.1$ ) and the conventional architecture ( $L_{nac}/r_{hi} = 3.8$ ), where positive values refer to aerodynamic benefits of the compact nacelle. Across the design space the NVF varies from + 1.2% to + 0.4% for the forward and close-coupled positions, respectively (Fig. 10(d)). This finding quantifies the expected benefits of compact UHBPR aero-engines over conventional configurations across a wide range of installation positions. While the vertical offset ( $dz/c$ ) has a negligible effect, the axial offset ( $dx/c$ ) is the dominant parameter. The compact aero-engine nacelle has a penalty in terms of  $NPF_{ins-cycle}$  with respect to the conventional architecture in the majority of installation positions (Fig. 10(a)). The largest deficit on  $NPF_{ins-cycle}$  is approximately of  $-0.9\%$  at the most close-coupled installation position. The variation on  $NPF_{ins-cycle}$  is accounted by the changes of the modified gross propulsive force and modified nacelle drag ( $D_{nac}^*$ ). Whilst compact aero-engine nacelles have a benefit on modified nacelle drag for forward positions with respect to conventional architectures

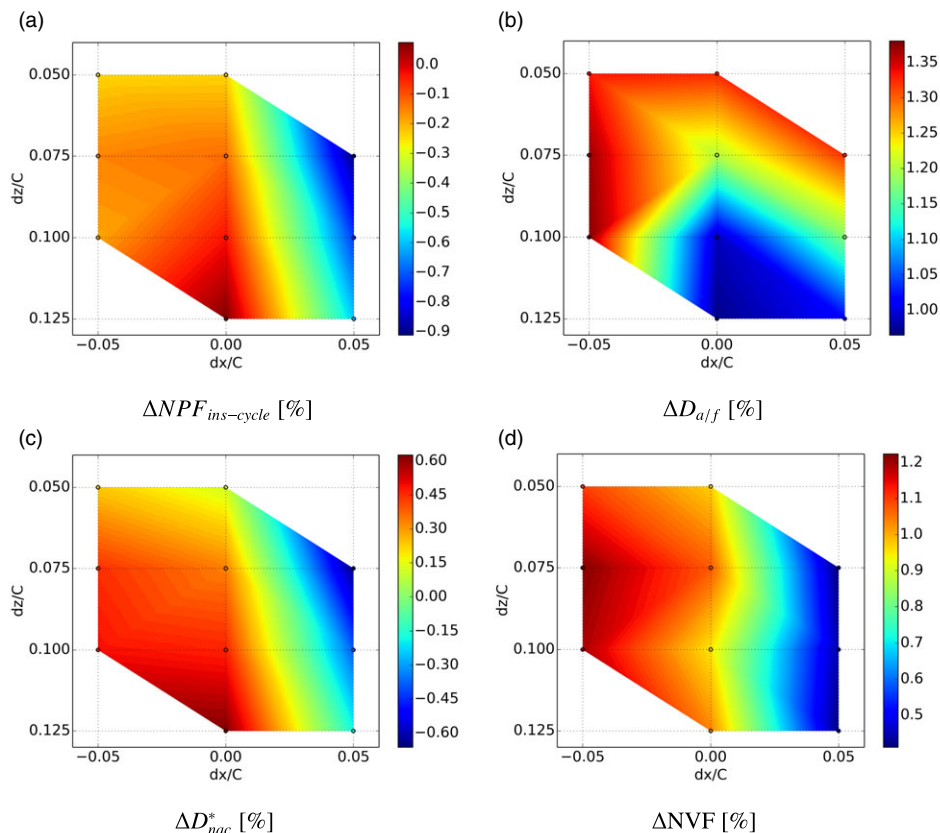


**Figure 10.** Difference ( $F_{compact} - F_{conventional}$ ) between the compact ( $L_{nac}/r_{hi} = 3.1$ ) and conventional ( $L_{nac}/r_{hi} = 3.8$ ) aero-engine nacelles across the design space investigated, where positive values are benefits and negative are penalties for the compact configuration. Results are normalised with the engine net thrust ( $F_N$ ).

( $L_{nac}/r_{hi} = 3.8$ ), there is a considerable penalty for close-coupled installation positions (Fig. 10(c)). This is caused by the adverse flow features that manifest at the rear of the compact aero-engine nacelle (Fig. 7). Regarding the airframe drag, there is a benefit between 1.0% and 1.35% for the compact nacelle architecture relative to the conventional aero-engine across the installation positions considered (Fig. 10(b)).

Figure 11 shows the normalised difference between the compact and conventional architectures on NVF and its constituent metrics at the selected installation positions of C, N, S, W and E. For example, for the forward position W, the benefit in net vehicle force of the compact nacelle configuration ( $L_{nac}/r_{hi} = 3.1$ ) is 1.19% (Fig. 11). It is similar to the benefit expected from the isolated aero-engines evaluation (Fig. 3), for which the reduction on isolated nacelle drag of 7.4% from conventional to compact aero-engine architecture (Fig. 3(a)) equals to an increment of 1.1% on the overall engine aerodynamic performance. Therefore, the expected benefits of designing isolated architectures are realised when the aero-engine is installed in forward installation positions, i.e. Position W. For this engine location there is a penalty on  $NPF_{ins-cycle}$  of  $-0.18\%$  which is produced by the reduction of the modified gross propulsive force as the modified nacelle drag has a benefit of 0.48% (Fig. 11). This benefit on  $D_{nac}^*$  is mainly caused by the reduction of the nacelle wetted area between  $L_{nac}/r_{hi} = 3.1$  and  $L_{nac}/r_{hi} = 3.8$  because no adverse flow-features are on the nacelle for this forward installation position. Lastly, the installation of the compact aero-engine nacelle in position W results in a reduction of the airframe drag by 1.38%.

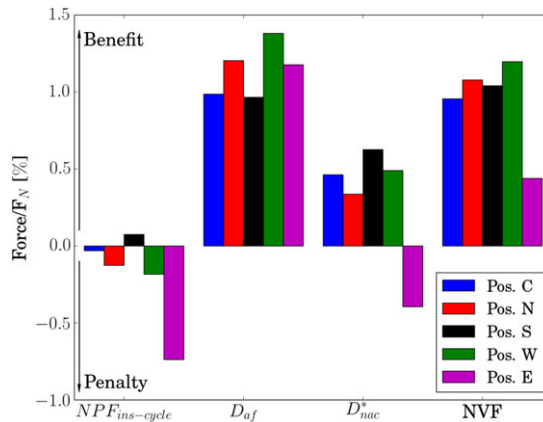


**Figure 11.** Breakdown of normalised forces. Difference between the compact ( $L_{nac}/r_{hi} = 3.1$ ) and conventional ( $L_{nac}/r_{hi} = 3.8$ ) aero-engine nacelles.

For the close-couple position E, the compact aero-engine has an overall increment in net vehicle force of 0.44% with respect to the conventional architecture (Fig. 11). It has a penalty on  $NPF_{ins-cycle}$  of 0.74%, which is partially accounted by the increment in modified drag by 0.39% due to the larger adverse interactions with the gully flow. Although for the long nacelle configuration ( $L_{nac}/r_{hi} = 3.8$ ) there is a flow reacceleration on the aft-end of the inboard side, the gully flow is not as severe as for the compact configuration (Fig. 7(b)). The civil future aero-engine nacelle ( $L_{nac}/r_{hi} = 3.1$ ) in the close-coupled installation positions results in a reduction of airframe drag ( $D_{af}$ ) by 1.17% with respect to the conventional architecture.

#### 4.0 Conclusions

This work has considered two powerplant configurations: a compact architecture that is representative of an ultra-high bypass ratio aero-engine, and a conventional turbofan. The effects of aircraft integration were evaluated across a range of installation positions for both aero-engines. A thrust-drag bookkeeping method has been employed to assess the overall aerodynamic performance of the airframe-powerplant in terms of net vehicle force (NVF) as well as its constituent metrics: net propulsive force, airframe drag and nacelle drag. For the compact nacelle architecture, the NVF varies by 1.7% across the investigated design space. The largest benefit was found for the most forward position and largest vertical offset. The aerodynamic differences between compact and conventional aero-engine nacelles across the different installation positions have been evaluated. Relative to the conventional configuration, the NVF on the compact aero-engine nacelle has a benefit of 1.2% at forward installation positions. Although the aerodynamic benefits obtained for isolated configurations are realised when the aero-engine is installed in forward installation positions, these performance improvements erode to 0.44% for close-coupled locations. This investigation has quantified the expected aerodynamic benefits of future compact UHBPR aero-engine nacelles with respect to conventional architecture. This work has also presented the changes in the flow characteristics along the powerplant and airframe, which has enabled to better understand the challenges of propulsion integration for future UHBPR aero-engines.

**Acknowledgment.** The authors thank Rolls-Royce plc for supporting this research. Due to commercial confidentiality agreements the supporting data is not available.

**Data availability statement.** Due to commercial confidentiality agreements the supporting data are not available.

**Competing interests.** The authors declares none.

## References

- [1] Birch, N.T. 2020 vision: The prospects for large civil aircraft propulsion, *Aeronaut. J.*, 2000, **104**, (1038), pp 347–352.
- [2] Tejero, F., Robinson, M., MacManus, D., and Sheaf, C. Multi-objective optimization of short nacelles for high bypass ratio engines, *Aerosp. Sci. Technol.*, 2019, **91**, pp 410–421.
- [3] Guha, A. Optimum fan pressure ratio for bypass engines with separate or mixed exhaust streams, *J. Propul. Power*, 2011, **17**, (5), pp 1117–1122.
- [4] Daggett, D., Brown, S., and Kawat, R. Ultra-efficient engine diameter study, Technical Report CR-2003-212309, NASA, 2003.
- [5] Waters, M.H. and Schairer, E.T. Analysis of turbofan propulsion system weight and dimensions, Technical Report TM X-73, NASA, 1977.
- [6] Wiart, L., Atinault, O., Paluch, B., Hue, D., and Grenon, R. Development of NOVA aircraft configurations for large engine integrations studies, In *33rd AIAA Applied Aerodynamics Conference, AIAA Paper 2015-2254*, 2015.
- [7] Sibilli, T., Savil, M., Sethi, V., MacManus, D., and Rolt, A. Numerical simulation of propulsion systems integration for very high bypass ratio engines, In *Proceedings of ASME Turbo Expo, GT2012-68908*, 2012.
- [8] Joo, G.W. Numerical investigation of installation effects in turbofan engines, *J. Propul. Power*, 2000, **16**, (4), pp 697–704.
- [9] Silva, V.T., Lundbladh, A., and Xisto, C. Aerodynamic installation effects of over-the-wing mounted ultra-high bypass engines, In *25th ISABE Conference*, 2022.
- [10] Magrini, A., Buosi, D., and Benini, E. Assessment of engine modelling on the installed aerodynamics of an ultra-high bypass turbofan, In *AIAA SciTech 2022 Forum, AIAA Paper 2022-0206*, 2022.
- [11] Jing, L., Zhenghong, G., Jiangtao, H., and Ke, Z.. Aerodynamic design optimization of Nacelle/Pylon position on an aircraft, *Chin. J. Aeronaut.*, 2013, **26**, (4), pp. 850–857.
- [12] Tejero, F., MacManus, D., Hueso-Rebassa, J., Sanchez-Moreno, F., Goulos, I., and Sheaf, C. Aerodynamic optimisation of future civil aero-engines by dimensionality reduction and multi-fidelity techniques, *Int. J. Numer. Methods Heat & Fluid Flow*, 2022.
- [13] Zhang, M.H., Meng, X.X., Wang, M.L., Wang, H., Bai, J.Q., and Nie, S.Y. Fluid mechanism analysis on the interaction between natural laminar flow Nacelle and Wingbody on a transonic aircraft, *AIP Adv.*, 2022, **12**, p 105323.
- [14] Palumbo, O., Palmer, D., Wall, T., Gulati, S., and Coder, J. Propulsion/airframe integration study for the placement of an ultra high bypass ratio turbofan on a slotted, natural laminar-flow wing, In *AIAA SciTech 2022 Forum, AIAA Paper 2022-2481*, 2022.
- [15] Schreiner, B.D.J., Tejero, F., MacManus, D., and Sheaf, C. Robust aerodynamic design of nacelles for future civil aero-engines, In *Proceedings of ASME Turbo Expo 2020: Turbomachinery Technical Conference and Exposition, GT2020-14470*, 2020.
- [16] Tejero, F., MacManus, D., Matesanz-Garcia, J., Swarouth, A., and Sheaf, C. Towards the design and optimisation of future compact aero-engines: Intake/Fan cowling trade-off investigation, *Int. J. Numer. Methods Heat & Fluid Flow*, 2022.
- [17] Vassberg, J., Dehaan, M., Rivers, M., and Wahls, R. Development of a Common Research Model for Applied CFD Validation Studies. In *26th AIAA Applied Aerodynamics Conference, AIAA Paper 2008-6919*, 2008.
- [18] Chau, T. and Zingg, D.W. Fuel burn evaluation of a transonic strut-braced-wing regional aircraft through multipoint aerodynamic optimization, *Aeronaut. J.*, 2023, **127**, (1308), pp 305–329.
- [19] Christie, R., Robinson, M., Tejero, F., and MacManus, D. The use of hybrid intuitive class shape transformation curves in aerodynamic design, *Aerosp. Sci. Technol.*, 2019, **95**, p. 105473, doi: [10.1016/j.ast.2019.105473](https://doi.org/10.1016/j.ast.2019.105473)
- [20] Goulos, I., Otter, J., Stankowski, T., Macmanus, D., Grech, N., and Sheaf, C. Design optimisation of separate-jet exhausts for the next generation of civil aero-engines, *Aeronaut. J.*, 2018, **122**, pp 1586–1605.
- [21] Otter, J. *Aerodynamics and performance of civil aero-engine exhaust systems*. PhD thesis, School of Aerospace, Transport and Manufacturing, Centre for Propulsion Engineering, Cranfield University, 2018.
- [22] Macmillan, W.L. *Development of a Module Type Computer Program for the Calculation of Gas Turbine Off Design Performance*. PhD thesis, Department of Power and Propulsion, Cranfield University, 1974.
- [23] Rivers, M.B. and Dittberner, A. Experimental Investigations of the NASA Common Research Model in the NASA Langley National Transonic Facility and NASA Ames 11-Ft Transonic Wind Tunnel (Invited). In *49th AIAA Aerospace Sciences Meeting including the New Horizons Forum and Aerospace Exposition, AIAA Paper 2011-1126*, 2011.
- [24] Vassberg, J.C., et al. Summary of the fourth AIAA computational fluid dynamics drag prediction workshop, *J. Aircr.*, 2014, **51**, (4), pp 1070–1089.
- [25] Levy, D.W., et al. Summary of data from the fifth computational fluid dynamics drag prediction workshop. *J. Aircr.*, 2014, **51**, (4), pp 1194–1213.
- [26] Goulos, I., Otter, J., Tejero, F., Rebassa, J.H., and MacManus, D. Civil turbofan propulsion aerodynamics: Thrust-drag accounting and impact of engine installation position, *Aerosp. Sci. Technol.*, 2020, **111**, p 106533.
- [27] Menter, F.R. Two-equation Eddy-viscosity turbulence models for engineering applications, *AIAA J.*, 1994, **32**, (8), pp 1598–1605.

- [28] Yufei, Z., Haixin, C., Song, F., Miao, Z., and Meihong, Z. Drag prediction method of powered-on civil aircraft based on thrust drag bookkeeping, *Chin. J. Aeronaut.*, 2015, **28**, pp 1023–1033.
- [29] Tejero, F., MacManus, D., Sanchez-Moreno, F. and Sheaf, C. Neural network-based multi-point, multi-objective optimisation for transonic applications. *Aerospace Science and Technology*, 2023, **136**, p. 108208.
- [30] Tejero, F., Goulos, I., MacManus, D., and Sheaf, C. Effects of aircraft integration on compact nacelle aerodynamics, In *AIAA SciTech 2020 Forum and Exposition, AIAA Paper 2020-2225*, 2020.